Applied Surface Science Advances 15 (2023) 100408

Contents lists available at ScienceDirect

Applied Surface Science Advances

journal homepage: www.sciencedirect.com/journal/applied-surface-science-advances

Doped $BaTiO_3$ cuboctahedral nanoparticles: Role of copper in photocatalytic degradation of dyes

P.I. Uma [a], U. Sandhya Shenoy [b,*], D. Krishna Bhat [a,*]

[a] Department of Chemistry, National Institute of Technology Karnataka, Surathkal, Mangalore 575025, India
[b] Department of Materials Science and Engineering, Institute of Engineering and Technology, Srinivas University, Mukka, Mangalore 574146, India

ARTICLE INFO

Keywords:
Barium titanate
Doping
Electronic structure
Photocatalyst
Copper
Dye degradation

ABSTRACT

The discovery of perovskite oxides as photocatalysts has opened unique possibilities for the degradation of pollutants such as dyes. In this work, we carry out both theoretical and experimental study for the design and preparation of copper doped $BaTiO_3$. To begin with, First principles electronic structure calculations revealed the presence of additional levels at the top of the valence band after doping copper, which considerably decreased the band gap making the oxide visible light active. Later, single pot synthesis of copper doped $BaTiO_3$ led to production of a material which was photocatalytically active in degrading both cationic and anionic dyes. From our work, we found that the photocatalyst 0.5 CuBTO decomposed 98.2% of methylene blue dye in 120 min and 99.4% of rose bengal dye within 45 min. Such high efficiency was attributed to the high surface area, appropriate band gap and low recombination rate of the charge carriers.

1. Introduction

Photocatalysis has emerged as an efficient way for environmental remediation in the past decades [1]. A photocatalyst should have a small bandgap so that it can absorb in the visible region and then photo generate charge carriers. The formed charged carriers should have enough separation to prevent recombination [2]. Due to their high catalytic performance and low cost, visible light active semiconductor photocatalysts are emerging as promising catalysts [3–8]. Many photocatalysts like TiO_2, CuO, ZnO, Fe_2O_3, $MTiO_3$ (M = Sr, Ca, Ba), CdS, ZnSe etc. are used to degrade dyes [3,7–19]. Titanate perovskites are mostly used due to their resemblance to TiO_2 [12,14]. The main disadvantage that makes the titanate perovskites inefficient is their wide bandgap that limits their applications in the UV region of the solar spectrum. Perovskite like $BaTiO_3$ is a versatile material with highly adaptable structural properties with a bandgap of 3.2 eV [14,20]. $BaTiO_3$ has long been known as the prototypical dielectric, thermoelectric and ferroelectric oxide, and is used in a variety of electronic devices, including multilayer capacitors, transducers, transistors and dynamic random-access memory devices [20]. Previously, by doping pristine $BaTiO_3$ with cations or anions, the bandgap was shifted into the visible region, making it a more efficient photocatalyst. Various elements like Ag, Ce, Cr, Fe, Mo, Mn, Ni, Rh, V, W and Zn are used as dopants that can shift the bandgap to the visible region for better efficiency [14,20–30]. Charge carrier recombination, which reduces photocatalyst efficiency, is a significant risk factor in narrowing the bandgap [14]. The doping should be in such a way that it should decrease the bandgap and simultaneously, the recombination rate must be low with a high charge carrier lifetime [3,31]. Since, most of these materials are used for hydrogen production rather than for photodegradation there is a wider scope for these doped $BaTiO_3$ being applied in the degradation of dyes. Mn doped $BaTiO_3$ photocatalyst showed 97.04% degradation of methylene blue (MB) in 360 min [21]. However, the time taken for complete degradation was very high. Hence, there is a need to find better dopants with greater efficiency. Copper, a transition metal ion is an ideal dopant that creates impurity levels decreasing the bandgap. The similar sizes of Cu^{2+} and Ti^{4+} also facilitates the substitutional doping.

We present here the results of an investigation of photocatalytic activity of Cu doped $BaTiO_3$ in degrading MB and rose bengal (RB) dye and provide fundamental insights using both experimental and theoretical approach. We performed a simple one-pot hydrothermal synthesis of pristine and copper doped $BaTiO_3$ without using the high temperature calcination method. Various characterizations revealed successful Cu incorporation and reduction in the bandgap, resulting in a visible light active photocatalyst. The previous reports of Rh doped $BaTiO_3$ revealed that when Rh shows mixed occupancy during doping,

* Corresponding authors.
E-mail addresses: sandhyashenoy347@gmail.com (U.S. Shenoy), denthajekb@gmail.com (D.K. Bhat).

https://doi.org/10.1016/j.apsadv.2023.100408
Received 21 February 2023; Received in revised form 30 March 2023; Accepted 30 April 2023
Available online 6 May 2023

recombination centres are created [14]. DFT results of the present work indicate the uniqueness of Cu by the fact that even with mixed occupancy, recombination centres are not created which was the biggest hurdle for doping strategy [3,14]. The efficient degradation of MB and RB dye confirms the photocatalyst as a versatile material for environmental remediation. In comparison to the 66% and 83% degradation of MB dye showed by Cu doped in $SrTiO_3$ prepared by Rahman et al. and V doped in $SrTiO_3$ prepared by Bantawal et al., respectively, 98.2% degradation was detected in 120 min in the present work [3,32]. While in V doped $SrTiO_3$, V acts an isovalent dopant in Ti site, here Cu acts as an aliovalent dopant in Ti site while favourably tuning the electronic structure [3]. The RGO/$SrTiO_3$ synthesized by Rosy and Kalpana degraded 90% of RB dye (0.2 ppm) within 120 min compared to 99.4% degradation of RB dye (10 ppm) within 45 min in the present work [33]. Also, the high cycling stability demonstrates the excellent efficiency of the material as a photocatalyst.

2. Materials and methods

2.1. Synthesis

Sigma Aldrich supplied all the chemicals, which were of analytical grade. Without any further purification, chemicals were used directly. Along with pristine $BaTiO_3$, doped samples of 5 different copper concentrations were prepared using the hydrothermal method of synthesis [34]. In 10 mL of isopropanol, 1.5 mL of titanium isopropoxide was dissolved. Calculated amount of copper acetate and barium hydroxide were added to this and magnetically stirred for about 30 min until completely dissolved. 15 mL of 5 M KOH solution was added dropwise. After the addition, the mixture was allowed to stir for 1 h. The resulting mixture was sealed in an autoclave and kept in an oven set to 150 °C for 24 h. To remove the impurities, the obtained mixture was washed with acetic acid and distilled water. The product was then dried in an oven at 70 °C overnight. The products obtained by using 0.25, 0.5, 0.75, 1.0, and 1.25 mol percent of the Cu precursor were labelled as 0.25 CuBTO, 0.5 CuBTO, 0.75 CuBTO, 1.0 CuBTO, and 1.25 CuBTO, respectively. Similarly, $BaTiO_3$ was prepared without the use of Cu precursor and labelled as BTO. The synthesis protocol of copper doped $BaTiO_3$ is shown in Scheme 1.

2.2. Characterization

We used an X-ray diffractometer (XRD, Rigaku Miniflex 600) equipped with monochromatic Cu K_α radiation (λ= 0.154 nm) at a scan rate of 2° per minute in the 2θ range of 20°- 80° to analyse the phase and purity of the produced materials. The surface morphology and nanostructure of the synthesized samples were analysed using transmission electron microscopy (TEM, FEI Tecnai G2 Spirit Bio- Twin TEM 120 kV). Omicron Nanotechnology Ltd. spectrometer equipped with an Al K_α source was used to record X-ray photoelectron spectrum (XPS). We determined the specific surface area using the Brunauer-Emmett-Teller (BET) method (Autosorb IQ-XR-XR, Anton Paar). The diffuse reflectance (DR) spectra were obtained using a UV–visible spectrometer (Perkin Elmer LAMBDA 950). The photoluminescence (PL) spectra (Fluoromax-4 Spectrofluorometer) were recorded at room temperature.

2.3. Determination of photocatalytic activity

A broadband high intensity discharge lamp (Philips MASTER Colour CDM-R/830) was used for measuring the photocatalytic activity as a visible light source. About 100 mL of dye solution (10 mg L^{-1}) and 25 mg of catalyst (for MB degradation) and 40 mg of the catalyst (for RB degradation) were taken in a crystallizing dish and sonicated for 10 min for uniform dispersion. The dish was loaded into the reactor and the light source was switched on after 30 min in dark to attain adsorption-desorption equilibrium [9]. 5 mL of the solution was taken in intervals of 30 min and spectrophotometrically analysed after centrifuging to remove the catalyst. A UV-visible spectrometer set to 664 nm for MB dye and 550 nm for RB dye was used to measure the absorbence of the supernatant dye solution. The percentage of degradation was calculated by Eq. (1).

$$\text{Degradation}\% = [(C_o - C) / C_o] \times 100 \quad (1)$$

where C_o is the initial concentration of the dye solution and C is the concentration at different intervals of time [14,35,36].

2.4. Computational details

We simulated the electronic structure of pristine and Cu doped $BaTiO_3$ using Quantum ESPRESSO package [37]. The first principles DFT calculations were carried out using 3 × 3 × 3 supercell (135 atoms) of primitive cubic $BaTiO_3$ in which Ba atoms occupy the corner, Ti the centre and O the face centres of the cube. A generalized gradient approximation with Perdew, Burke and Ernzerhof (PBE) functional type was used to exchange the correlation energy [38]. The ultrasoft pseudopotential considered $5s^2 5p^6 6s^2$, $3s^2 3p^6 3d^2 4s^2$, $2s^2 2p^4$, $3d^{10} 4s^1$ of Ba, Ti, O and Cu, respectively as the valence electrons. The wave functions represented by the plane wave basis were terminated with an energy and charge density cut-off of 90 Ry and 720 Ry, respectively. A k point mesh of 3 × 3 × 3 and 6 × 6 × 6 was used to sample the Brillouin zone for self-consistent and non-self-consistent field calculations, respectively. The electronic structure was determined along Γ - X - M - Γ - R - X high symmetry path.

3. Results and discussion

3.1. XRD analysis

The XRD patterns show that pristine and doped $BaTiO_3$ are formed completely without any impurities (Fig. 1). The crystal structures coincide with the standard perovskite phase of $BaTiO_3$ (JCPDS card no. 1–074–1962). The calculated lattice parameter increases from 4.032 Å to 4.047 Å as we increase the doping from 0 to 1.25 mol%. We also observe that the peaks shifts towards lower 2θ values for the doped samples compared to the undoped perovskite oxide (Fig. S1). When a dopant has a larger ionic radius than the host lattice, it causes tensile

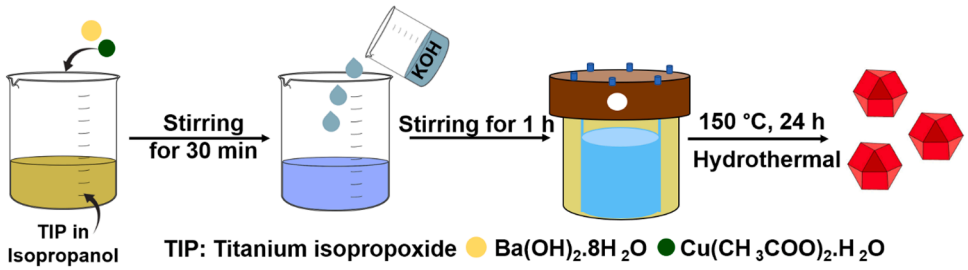

Scheme 1. Schematic representation of the synthesis of copped doped $BaTiO_3$.

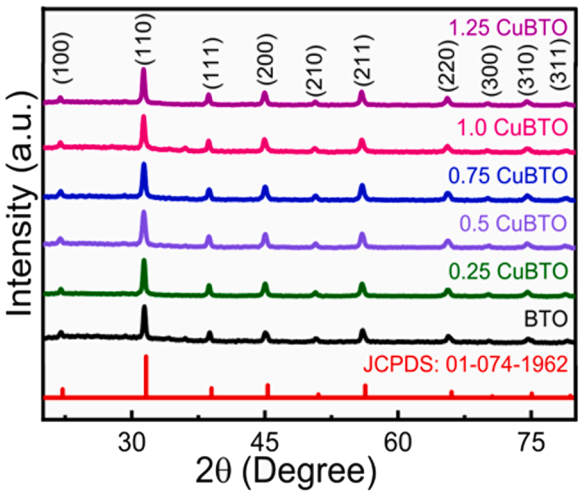

Fig. 1. XRD patterns of $BaTiO_3$ and Cu-doped $BaTiO_3$ with varying concentrations of Cu in comparison to the standard data.

strain in the lattice, increasing the lattice parameter and lowering the 2θ value. This confirms Cu^{2+} incorporation into the Ti^{4+} site as the ionic size of the former is larger than the latter. This is also supported by the fact that thermodynamically Ti site is more preferred than Ba site as the amount of strain induced if Cu occupies Ba site would be much higher due to larger size disparity between Cu^{2+} (72 pm) and Ba^{2+} (135 pm) in comparison to Cu^{2+} (72 pm) and Ti^{4+} (68 pm).

3.2. XPS analysis

The presence of elements like Ba, Ti, O and Cu and their oxidation states were elucidated from XPS analysis of 0.5 CuBTO. The two spin states of Ba 3d i.e. Ba $3d_{5/2}$ and Ba $3d_{3/2}$, appear at binding energies of 779.3 eV and 794.7 eV, respectively (Fig. 2a) [14,39]. The binding energy difference of 15.4 eV between the two spin states of Ba proved that the oxidation state of Ba in $BaTiO_3$ is +2. The binding energies of 459.05 eV (for Ti $2p_{3/2}$) and 464.8 eV (for Ti $2p_{1/2}$), respectively in Fig. 2b indicates that Ti is in the +4 oxidation state [14,40]. Furthermore, the lattice oxygen (O_L) and surface hydroxyl groups (O_{OH}) can be attributed to the peaks with binding energies of 530.10 eV and 531.80 eV, respectively (Fig. 2c) [41,42]. The deconvoluted peaks of Cu at binding energies of 932.12 eV and 950.03 eV can be allotted to the Cu $2p_{3/2}$ and Cu $2p_{1/2}$ spin states, respectively, i.e. Cu exists as Cu^{2+} in copper doped $BaTiO_3$ (Fig. 2d) [43,44].

3.3. Morphology and surface area analysis

We studied the morphology of the samples using TEM and observed a cuboctahedral shape for both undoped (Fig. S2) and doped $BaTiO_3$ (Fig. 3a) samples indicating that doping of Cu does not change the morphology of the samples. We observed the 101 planes in the HRTEM image of 0.5 CuBTO sample (Fig. 3b) with the lattice fringes having a

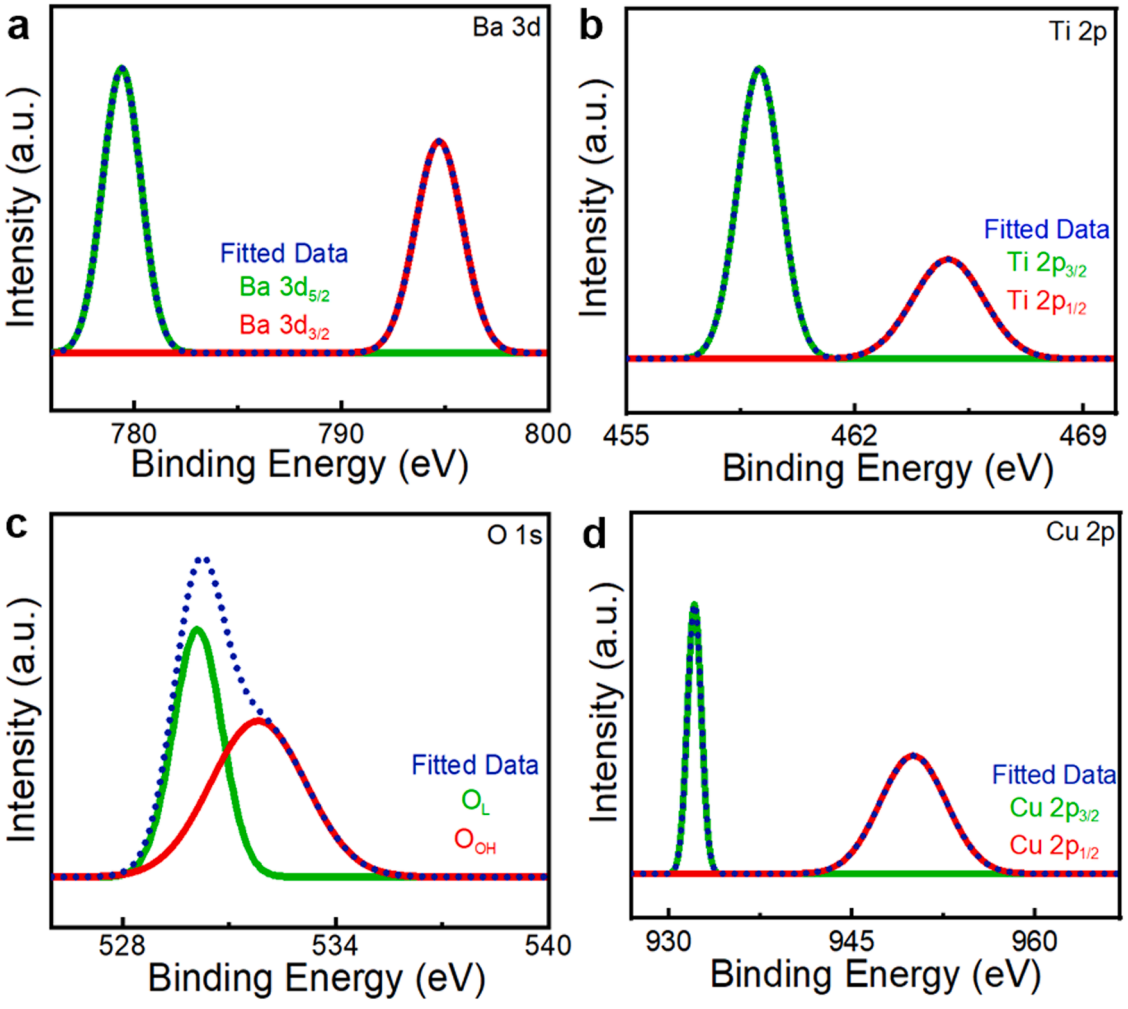

Fig. 2. High-resolution XPS plot of 0.5 CuBTO (a) Ba 3d, (b) Ti 2p, (c) O 1 s and (d) Cu 2p.

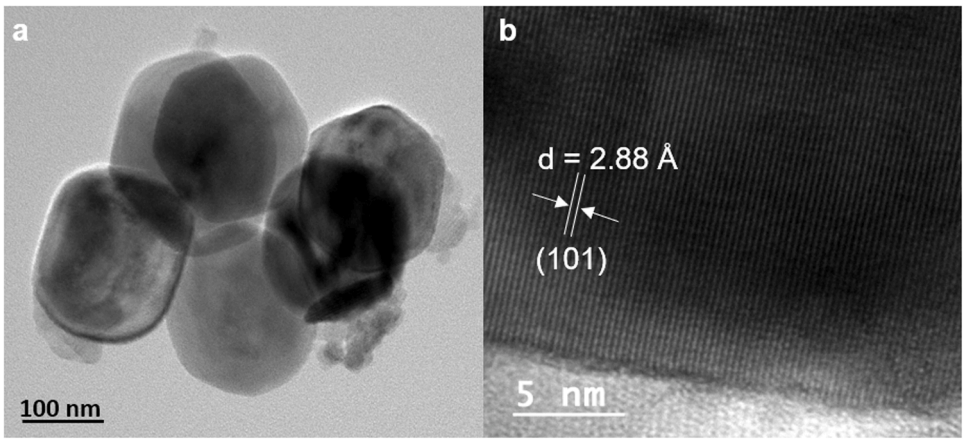

Fig. 3. (a) TEM image and (b) HRTEM image of 0.5 CuBTO.

d spacing equal to 2.88 Å. The interplanar distance calculated from HRTEM is in accordance with the d value of the 101 planes from XRD results (2.85 Å). The elemental composition studied using EDX reveals Ba, Ti, O and Cu as the elements present in 0.5 CuBTO, confirming the results from XPS (Fig. S3).

We studied the surface area of the synthesized samples as it plays a vital role in the photocatalysis. The morphology of the sample decides the surface area to a large extent. Cuboctahedran shape has 8 triangular faces and 6 square faces with 24 edges and facilitates better adsorption and photocatalytic degradation of dyes on the surface. A type IV pattern isotherm was observed in the nitrogen adsorption-desorption isotherms of $BaTiO_3$ and 0.5 CuBTO samples with hysteresis loops being type H3, indicating the presence of slit-like mesopores (Fig. 4) [45]. The values of average pore diameter of the 0.5 CuBTO sample indicated the presence of mesopores and macropores. The BET surface area was found to be 30.902 m^2/g for the 0.5 CuBTO sample, which is slightly higher than that of pure $BaTiO_3$ having a surface area of 29.655 m^2/g. The closer values are due to unaltered morphology of the sample even after doping. The pore volume of the 0.5 CuBTO sample was found to be 0.112 cc/g which is greater than that of the pristine sample (0.110 cc/g). The high pore volume is crucial in the diffusion of molecules for the efficient photocatalysis.

3.4. Electronic structure analysis

The electronic structure of $BaTiO_3$ reveals a direct band gap of 1.88 eV at Γ point which is close to previously reported values of 1.92 eV and 1.93 eV for pristine $BaTiO_3$ with 2 × 2 × 2 supercell dimensions [14,20]. The underestimation of band gap observed here is well documented previously in electronic structure calculations due to the existence of a discontinuity in derivative of energy with respect to number of electrons [20,46]. Two indirect band gaps of 1.76 eV and 1.74 eV between M → Γ and R → Γ, respectively is also observed in the electronic structure (Fig. 5a) [20]. The partial density of states (pDOS) reveals that the valence and conduction states of pristine $BaTiO_3$ are formed by 'p' orbitals of oxygen and 'd' orbitals of Ti, respectively (Fig. 5b). To study the effect of site occupancy in Cu doped $BaTiO_3$ we simulated 3 cases. Case 1: by replacing one Ba atom with Cu atom, case 2: by replacing one Ti atom with Cu atom and case 3: by replacing one Ba atom and one Ti atom with two Cu atoms. We observe that substitution of Ba with Cu leads to introduction of an addition level at the edge of the valence band decreasing the direct band gap at Γ point to 1.77 eV and indirect band gaps to 1.69 eV and 1.68 eV between M → Γ and R → Γ, respectively (Fig. 5c). This donor level is formed by the hybridization of Cu 'd' orbitals with 'p' orbitals of O, appearing as a sharp peak near the Fermi level in the pDOS plot (Fig. 5d). The width of this donor level increases with the increase in the amount of doping as seen in Fig. 5e, when 2 Ba atoms are replaced with 2 Cu atoms. The intensity of the donor peak is seen to increase with the increase in the concentration of Cu (Fig. 5f).

Substitution of Ti by Cu leads to decrease in the band gap to 1.73 eV. Both the indirect band gaps decrease to 1.37 eV due to the lifting up of states near M and R points (Fig. 6a). The hybridization of 'p' orbitals of O with 'd' orbitals of Cu appears as a doublet peak in the pDOS plot which is flatter in nature compared to the case where Cu substitutes Ba (Fig. 6b). The increase in the concentration of Cu in Ti sites leads to increase in the dispersion of the bands with increase in the band width of the donor levels and increase in the height of DOS peaks (Fig. 6c–f).

Since at higher concentrations there is possibility of dopant atoms

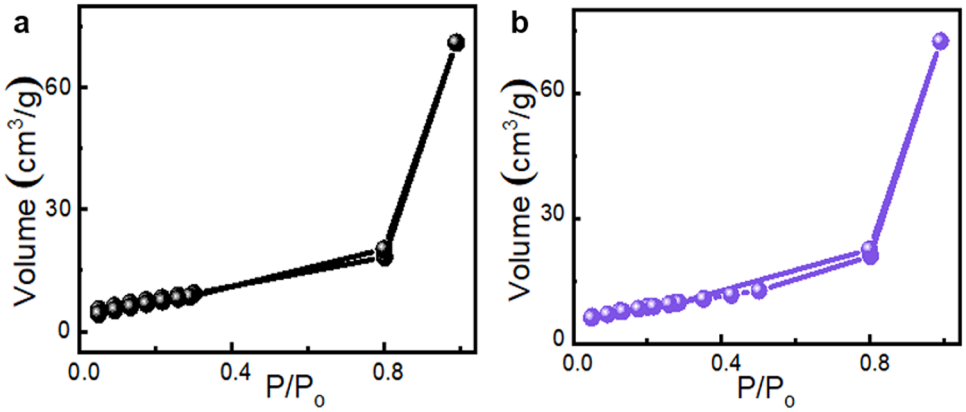

Fig. 4. BET surface area analysis of the (a) $BaTiO_3$ and (b) 0.5 CuBTO sample.

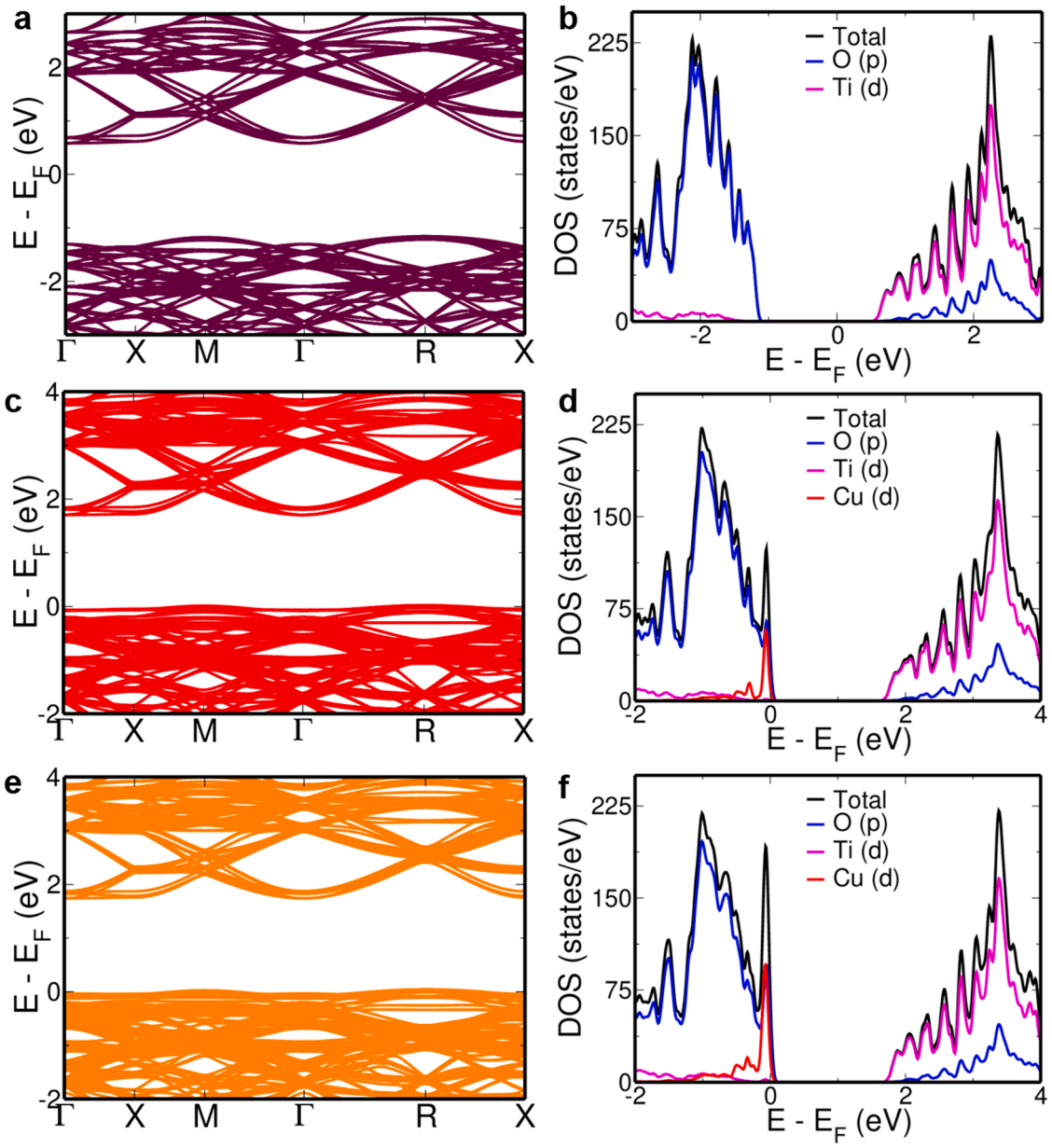

Fig. 5. Electronic structure and pDOS of (a and b) $BaTiO_3$, (c and d) Cu doped $BaTiO_3$ with one Cu in Ba site, (e and f) Cu doped $BaTiO_3$ with two Cu in Ba sites.

going into both Ba and Ti site, we simulated such a configuration keeping the dopants at the farthest distance from each other in $3 \times 3 \times 3$ supercell (Fig. 7a) [47,48]. In this case the estimated band gap is 1.80 eV, higher than in the case of doping at Ba site and Ti site alone (Fig. 7b). Further, the indirect band gaps decrease to 1.46 eV and 1.47 eV between $M \rightarrow \Gamma$ and $R \rightarrow \Gamma$, respectively lying in between that of case 1 and case 2. The electronic structure and pDOS shows the combined features of single site doping cases (Fig. 7c). This is quite different from the case of Rh doped $BaTiO_3$ and $SrTiO_3$ where mixed occupancies led to formation of recombination centers [14,31]. The DFT results indicate that doping of copper leads to decrease in the band gap due to introduction of donor states just above the valence band edge extending the absorption towards visible light region irrespective of the site occupied. It also reveals that doping in Ti site alone leads to higher reduction in the band gap making it the preferred site.

3.5. Optical absorption analysis

In the DR spectra of pristine $BaTiO_3$, we observe that an absorption edge appears at around 395 nm due to the electronic transitions from valence band to conduction band which is in fact transitions from the O 'p' orbitals to the Ti 'd' orbitals as suggested by the pDOS calculations (Fig. 8a) [14]. As revealed by the DFT studies, doping results in the formation of new states just above the valence of $BaTiO_3$ which act as donor levels and causes a decrease in the bandgap. Due to this decrease in the bandgap caused by the doping, the absorption edges of Cu-doped samples red-shift to the visible region. The absorption data was derived using the Kubelka-Munk equation (Eq. (2)).

$$\alpha = A \Big/ S = \frac{(1-R)^2}{2R} \tag{2}$$

Where α is Kubelka-Munk function, R is the reflectance, A and S are the absorption and scattering coefficients [3]. The bandgap was determined using Tauc method by plotting $(\alpha \cdot h\nu)^{1/\gamma}$ vs band gap energy ($h\nu$), where γ is ½ for direct transition band gaps and 2 for indirect transitions (Fig. S4) [49]. The bandgaps of $BaTiO_3$, 0.25 CuBTO, 0.5 CuBTO, 0.75 CuBTO, 1.0 CuBTO and 1.25 CuBTO were found to be 3.16 eV, 2.97 eV,

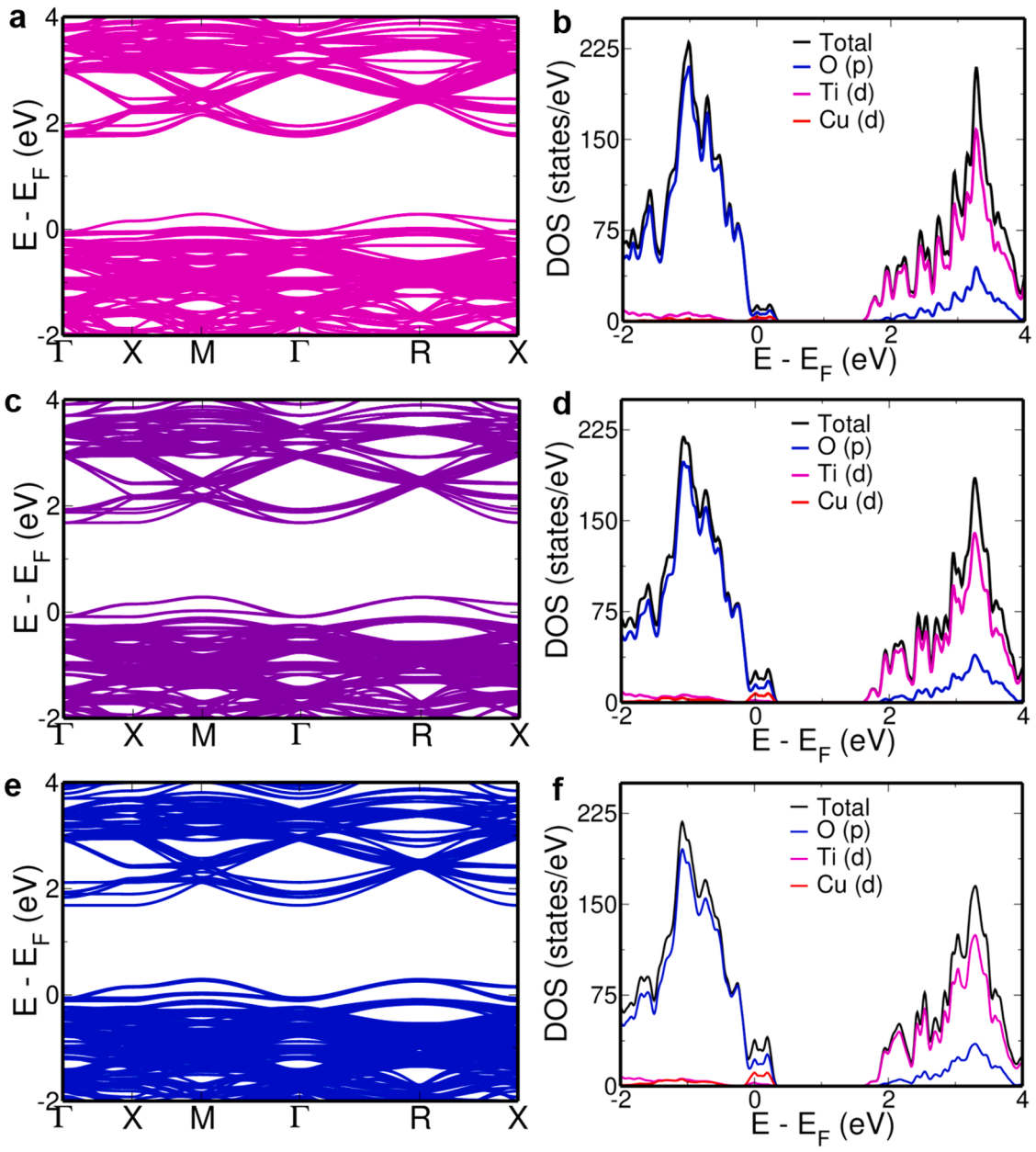

Fig. 6. Electronic structure and pDOS of (a and b) Cu doped $BaTiO_3$ with one Cu in Ti site, (c and d) Cu doped $BaTiO_3$ with two Cu in Ti sites, (e and f) Cu doped $BaTiO_3$ with three Cu in Ti sites.

2.92 eV, 2.89 eV, 2.85 eV and 2.80 eV, respectively. Due to the increase in the width of the donor level introduced by Cu dopant, which moves closer towards the conduction band, we see a red shift in the absorption peak accompanied by a drop in the bandgap with an increase in the concentration of Cu doping [14]. Thus doping converted the catalysts to be visibly active making the decomposition of contaminants feasible in the visible region.

The sudden drop in the fluorescence intensity for the Cu doped samples compared to that of the pristine sample observed in the PL spectra indicates the lower possibility for the recombination of photo-induced charges in the case of doped samples (Fig. 8b). The PL intensity decreases up to 0.5 CuBTO, then increases as the concentration of dopant increases. The PL studies confirm that doping of pristine perovskite with Cu decreased the bandgap without increasing the recombination rate, demonstrating the effect of doping on increasing the photocatalyst's efficiency [35].

3.6. Photocatalytic activity

We used MB dye to study the photocatalytic degradation of CuBTO under visible light. The activity in the absence of light indicates the effect of adsorption of the dyes while that in the presence of light indicates the photocatalytic activity of the samples (Fig. 9a). In the absence of the catalyst, the efficiency of the degradation of the samples was very less proving the importance of the catalyst. Moreover, the doped samples showed much higher efficiency than the pristine samples. With the lower bandgap catalyst, the absorption of light becomes easier and thus the efficiency increases. Amongst the doped samples, 0.5 CuBTO showed the highest degradation efficiency of 98.2% within 120 min for the MB dye. The efficiency decreased with the increase in Cu concentration after 0.5 mol% of Cu precursor as predicted by the PL results. The degradation efficiency and the PL intensity relate well in such a manner that lower fluorescence intensity suggests lower recombination and thus higher degradation efficiency. In addition to it, the 0.5 CuBTO sample also

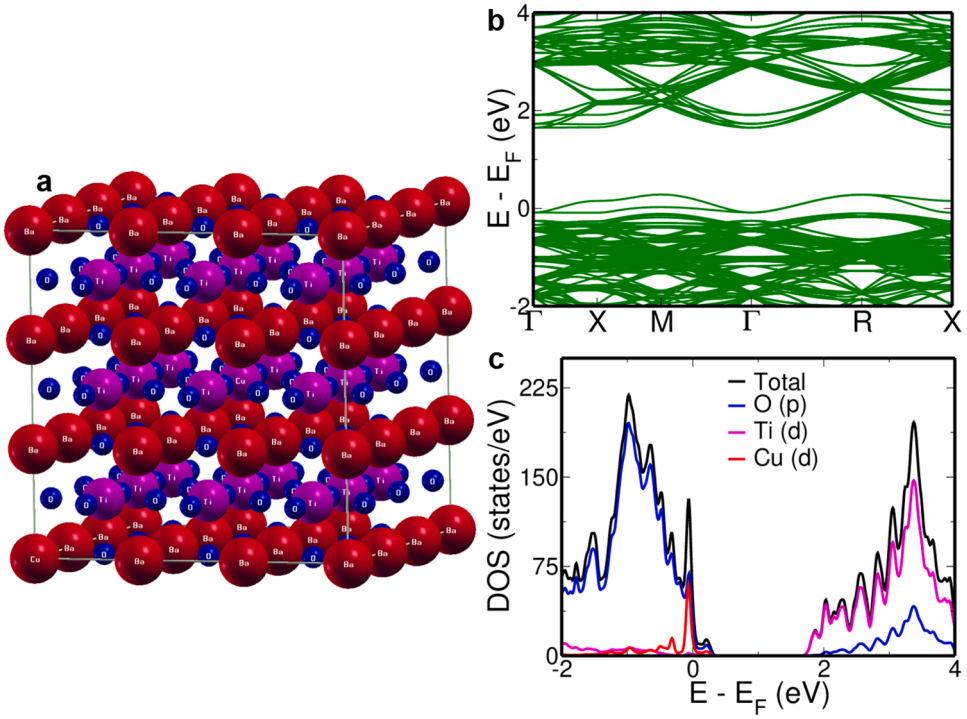

Fig. 7. (a) Crystal structure, (b) Electronic structure and (c) pDOS of Cu doped $BaTiO_3$ with one Cu in Ba site and one in Ti site.

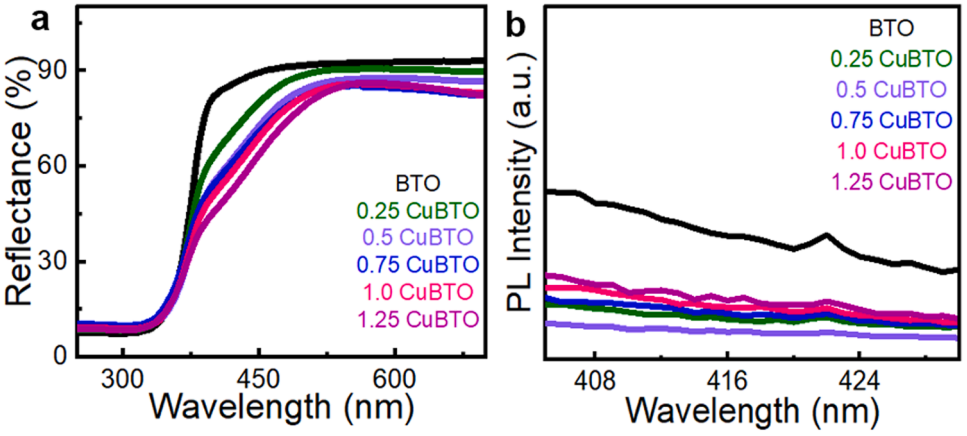

Fig. 8. (a) UV-visible DR spectra; (b) PL spectra of $BaTiO_3$ and Cu-doped $BaTiO_3$ samples.

showed a higher surface area increasing the chance of higher adsorption of dyes onto the surface of the catalyst leading to better degradation.

The kinetics of the photocatalytic degradation of MB by $BaTiO_3$ and Cu-doped $BaTiO_3$ is in good agreement with the pseudo first-order rate Eq. (3) given by,

$$-\ln(C/C_o) = kt \quad (3)$$

where C_o is the initial concentration of dye, C is the concentration of the dye at irradiation time (t) and k is the first order rate constant. k, in turn, is calculated from the slope of the straight-line plot of $-\ln(C/C_o)$ versus t [3,35]. The degradation kinetics of MB, revealed the higher efficiency of 0.5 CuBTO compared to the other samples by virtue of its higher value of rate constant (Fig. 9b).

Trapping experiments were used to identify the active species involved in photocatalytic degradation [3]. The procedure was similar to that used for degradation measurements above, but different radical scavengers were added, including benzoquinone (1 mM) as a superoxide anion radical (O_2^-) scavenger, potassium iodide (10 mM) as a hole (h^+) scavenger, and isopropyl alcohol (10 mM) as a hydroxyl radical (OH^-) scavenger [40]. The experiments show that superoxide radical anions are not the active species, as the addition of benzoquinone had little effect on photocatalytic activity (Fig. 9c) [14]. When potassium iodide (a hole scavenger) and isopropyl alcohol (an OH^- scavenger) were added, photocatalytic activity was significantly reduced. As a result, the active species in the effective degradation of dye was found to be holes and hydroxyl radicals [3].

The high stability of 0.5 CuBTO is further confirmed by the cyclic stability test for 7 cycles indicating the photo corrosion resistance (Fig. 9d) [50]. We examined the XRD pattern of doped $BaTiO_3$ after the degradation reaction to see if the photocatalyst changed after being exposed to visible light. The XRD pattern was identical before and after the degradation reaction, with no changes in the peaks (Fig. 10). This demonstrates the catalyst's stability because no structural changes occur after the reaction.

The Eyring equation and activation complex theory (ACT) was used

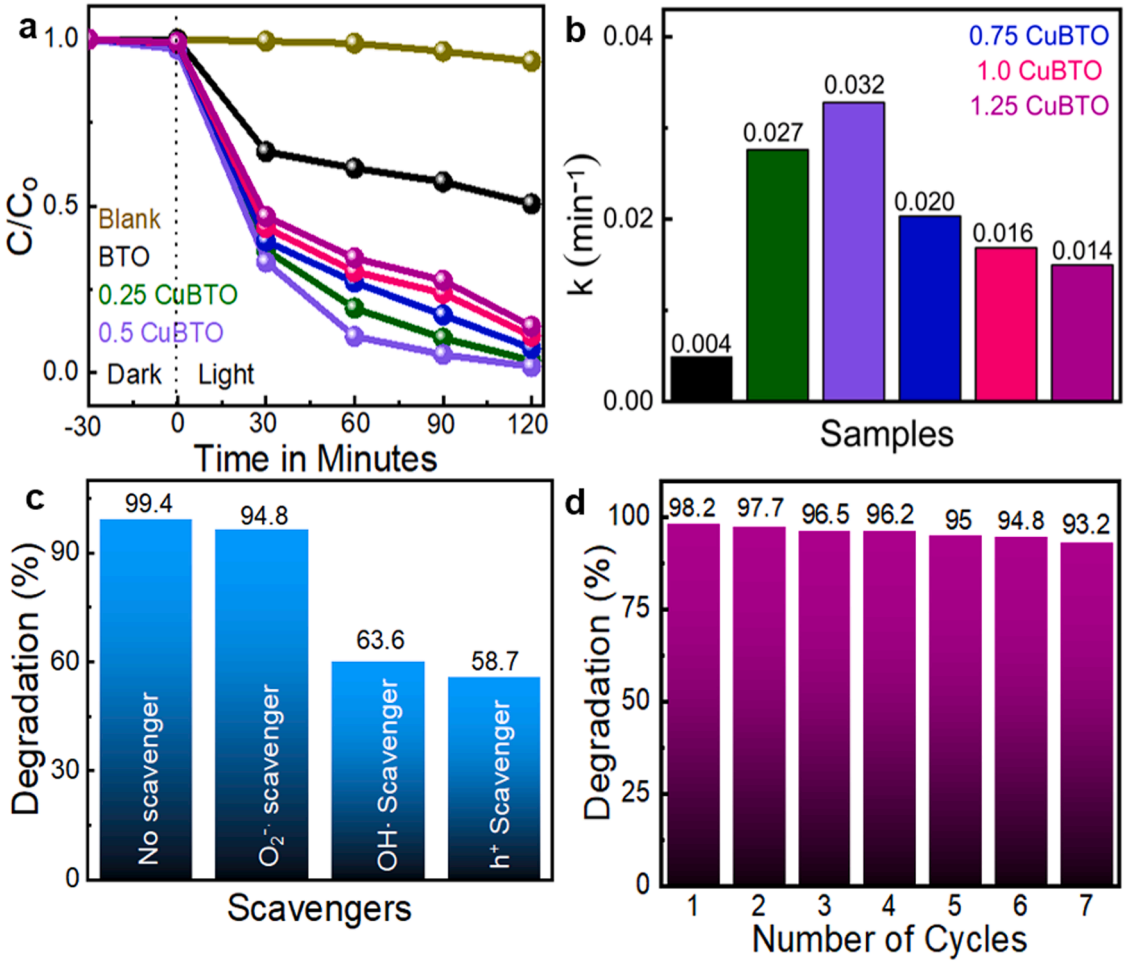

Fig. 9. (a) The photocatalytic degradation of MB, (b) Rate constants of the photocatalytic degradation of MB by the synthesized $BaTiO_3$ and Cu-doped $BaTiO_3$, (c) Effect of radical scavengers on the photocatalytic degradation of MB by 0.5 CuBTO, (d) Cyclic stability test of 0.5 CuBTO.

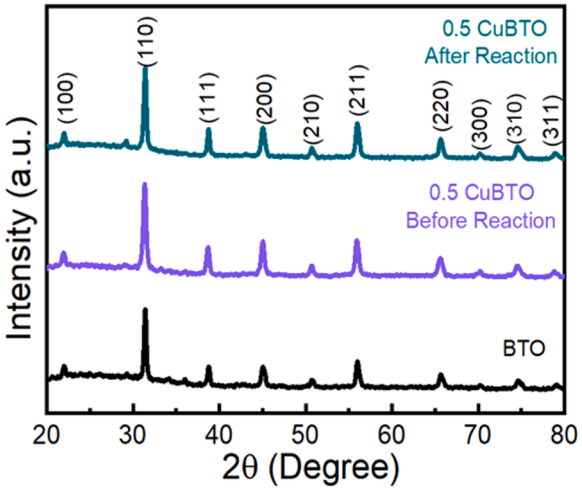

Fig. 10. XRD patterns of Cu-doped $BaTiO_3$ before and after degradation.

to calculate thermodynamic properties such as the energy of activation (E_a), free energy of activation ($G^{\#}$), enthalpy of activation ($H^{\#}$), and entropy of activation ($S^{\#}$) [51]. Table 1 shows the thermodynamic parameters of MB degradation. According to Table 1, photodegradation without a catalyst requires more activation energy than photodegradation with $BaTiO_3$ and Cu doped $BaTiO_3$. The 0.5 CuBTO sample has the lowest activation energy, activation enthalpy, and free energy of activation. Lower values indicate that the catalyst alters the reaction pathway, resulting in a high rate of reaction. Because both the free energy of activation and the enthalpy of activation is positive, the reaction is endothermic and non-spontaneous.

Table 1
Thermodynamic parameters of $BaTiO_3$ and Cu doped $BaTiO_3$ samples for the degradation of MB dye.

Sample	E_a (kJ mol^{-1})	$\Delta H^{\#}$ (kJ mol^{-1})	$\Delta S^{\#}$ (kJ mol^{-1})	$\Delta G^{\#}$(kJ mol^{-1})
Without catalyst	15.5	13.0	−0.25	89.0
$BaTiO_3$	13.3	10.8	−0.25	86.7
0.25 CuBTO	9.0	6.5	−0.25	82.5
0.5 CuBTO	**8.6**	**6.1**	**−0.25**	**82.0**
0.75 CuBTO	9.7	7.3	−0.25	83.2
1.0 CuBTO	10.3	7.8	−0.25	83.8
1.25 CuBTO	10.6	8.1	−0.25	84.1

To study if the same catalyst can be used for the degradation of other dyes, we carried out photocatalytic degradation experiments on RB dye. Since MB was a cationic dye, RB was chosen to study the effect on anionic dye. The RB dye degraded within 45 min and a significant degradation of 99.4% was observed in the case of 0.5 CuBTO (Fig. 11). The anionic RB dye at the pH range of 6–8 is in its protonated form, thus having greater interaction with the negatively charged photocatalyst surface [52]. This stronger interaction yields a better photocatalytic

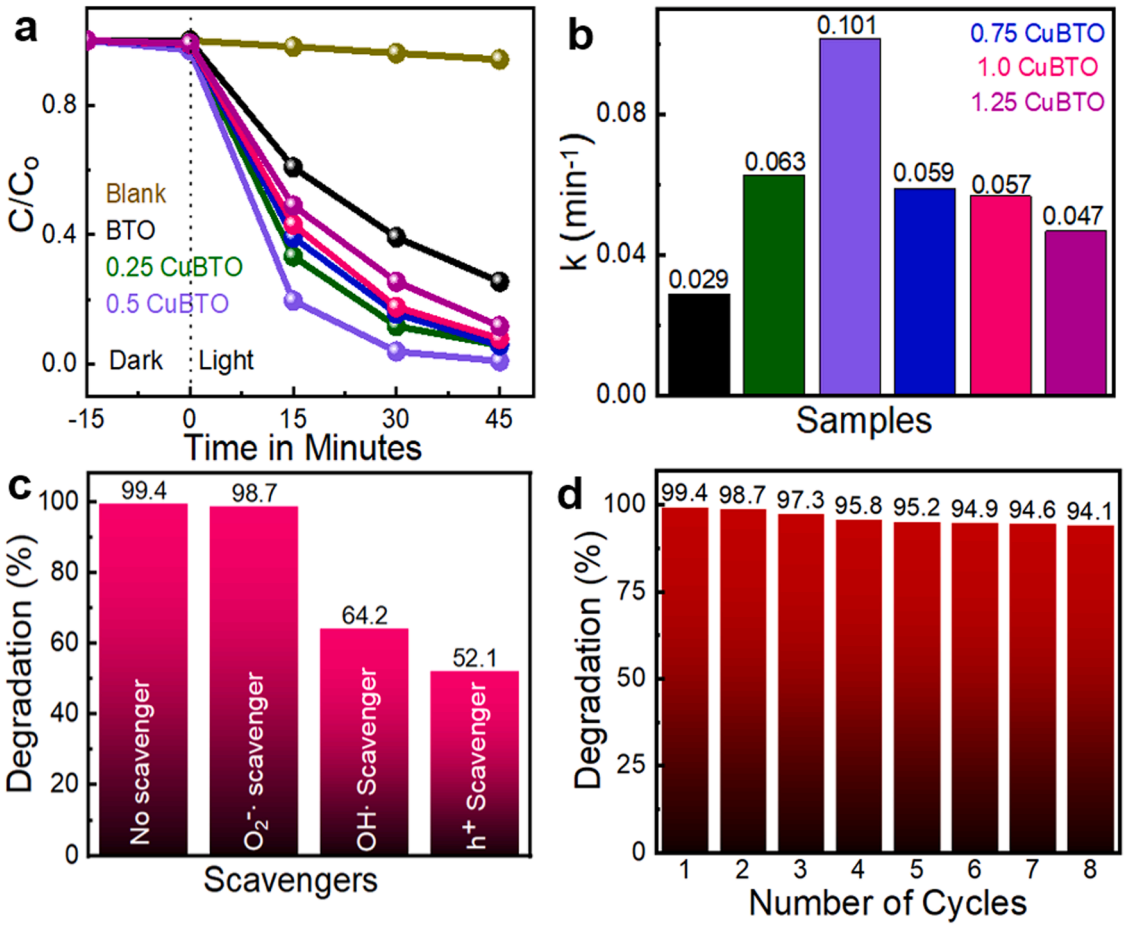

Fig. 11. The photocatalytic degradation of RB, (b) Rate constants of the photocatalytic degradation of RB by the synthesized $BaTiO_3$ and Cu-doped $BaTiO_3$, (c) Effect of radical scavengers on the photocatalytic degradation of RB by 0.5 CuBTO, (d) Cyclic stability test of 0.5 CuBTO.

degradation efficiency. Trapping experiments results mimicked the trend of MB dye results (Fig. 11c). Further, the cyclic stability of the catalyst was found to be high, even in the case of RB degradation (Fig. 11d). The trend in the thermodynamic parameters also was similar to that of MB degradation (Table 2). The photocatalyst can thus degrade both the anionic and cationic dyes and can be termed a versatile semiconductor photocatalyst [33].

Based on the above results, a mechanism for the photodegradation of dye is proposed (Fig. 12). Absorption of light transfers energy to the molecule, exciting electrons from the valence band to the conduction band. Electron migration from the valence band results in positive holes in the valence band and electrons in the conduction band [53]. The excited electrons can reduce any substance or react with electron acceptors such as O_2 to form a superoxide radical anion ($O_2^{\cdot-}$). The hole can directly oxidize the dye or react with OH^- or H_2O, oxidizing it to hydroxyl radicals ($OH^{\cdot}$). These formed radicals are so reactive and can attack aromatic rings of the dye leading to degradation. The MB dye undergoes degradation by the attack of the formed reactive oxygen species ($OH^{\cdot}$, $O_2^{\cdot-}$) via several steps. The first step is demethylation followed by breaking the central aromatic ring of MB. This is followed by the breakage of side aromatic rings. Then the fragments produced from the rupture of the aromatic rings are converted into intermediate species like $R\text{-}NH^{3+}$, phenol, aniline and aldehydic/carboxylate species. Finally, these intermediates are converted into simpler molecules such as CO_2, H_2O, SO_4^{2-} and NH^{4+} [54,55]. Similarly the radicals oxidize RB into its colourless leuco form and further degradation to harmless products [33]. Thus the synthesized materials act as an efficient photocatalyst for the degradation of MB and RB dye and the material can be tested for other pollutants as well.

Table 2
Thermodynamic parameters of $BaTiO_3$ and Cu doped $BaTiO_3$ samples for the degradation of RB dye.

Sample	E_a (kJ mol^{-1})	$\Delta H^{\#}$ (kJ mol^{-1})	$\Delta S^{\#}$ (kJ mol^{-1})	$\Delta G^{\#}$(kJ mol^{-1})
Without catalyst	20.2	17.7	−0.25	93.7
$BaTiO_3$	8.8	6.3	−0.25	82.4
0.25 CuBTO	6.9	4.4	−0.25	80.4
0.5 CuBTO	**5.7**	**3.2**	**−0.25**	**79.1**
0.75 CuBTO	7.0	4.5	−0.25	80.5
1.0 CuBTO	7.1	4.6	−0.25	80.6
1.25 CuBTO	7.6	5.1	−0.25	81.1

4. Conclusion

A one-pot hydrothermal approach was used to successfully synthesize a highly efficient copper doped $BaTiO_3$ photocatalyst. The photocatalyst was found to be suitable for both cationic and anionic dye photodegradation. The characterizations reveal the effective doping of Cu in $BaTiO_3$. The high surface area of 30.902 m^2/g for the 0.5 CuBTO sample resulted in the catalyst's high performance. The decrease in the bandgap to the visible region greatly increased photocatalytic activity. Although the highest doped sample has the smallest bandgap, it performed poorly due to the presence of recombination centres at higher dopant concentrations, which may have decreased efficiency. Thus, the absence of recombination centres, high surface area, and lower bandgap of the 0.5 CuBTO sample improved photocatalytic activity, with 98.2%

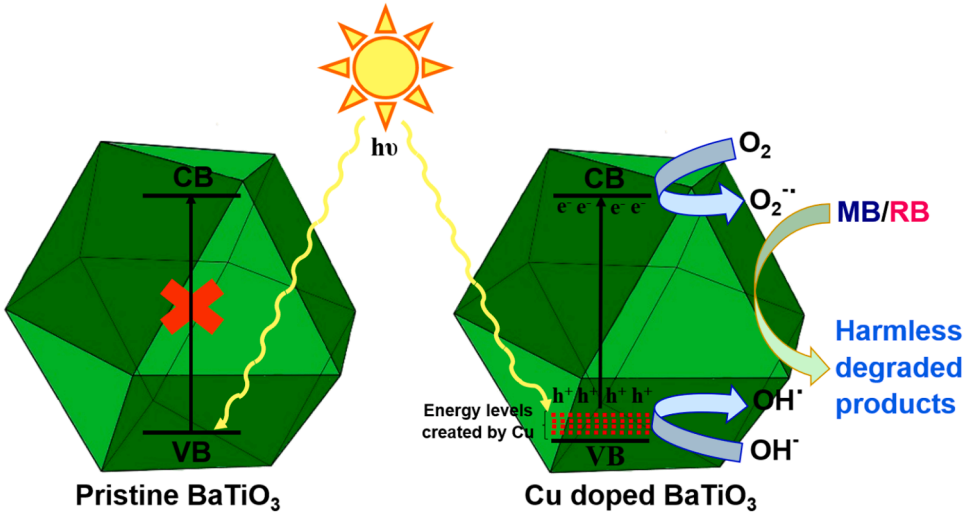

Fig. 12. The photocatalytic mechanism for the degradation of dye by Cu doped $BaTiO_3$ under visible light irradiation.

MB degradation in 120 min and 99.4% RB degradation in 45 min. This strategy could be extended to other perovskites to improve their photocatalytic efficiency to photodegrade dyes, which are toxic to the ecosystem.

Declaration of Competing Interest

The authors declare that they have no known competing financial interests or personal relationships that could have appeared to influence the work reported in this paper.

Data availability

Data will be made available on request.

Acknowledgement

The author USS acknowledges the financial support received from Science and Engineering Research Board, Government of India under SRS scheme.

Supplementary materials

Supplementary material associated with this article can be found, in the online version, at doi:10.1016/j.apsadv.2023.100408.

References

[1] M.M.J. Sadiq, U.S. Shenoy, D.K. Bhat, Enhanced photocatalytic performance of N-doped RGO-$FeWO_4$/Fe_3O_4 ternary nanocomposite in environmental applications, Mater. Today Chem. 4 (2017) 133–141.
[2] W. Chen, G.B. Huang, H. Song, J. Zhang, Efficient and stable charge transfer channels for photocatalytic water splitting activity of CdS without sacrificial agents, J. Mater. Chem. A 8 (2020) 20963–20969.
[3] H. Bantawal, U.S. Shenoy, D.K. Bhat, Vanadium-doped $SrTiO_3$ nanocubes: insight into role of vanadium in improving the photocatalytic activity, Appl. Surf. Sci. 513 (2020), 145858.
[4] J. Li, X. Liu, J. Zhang, Smart assembly of sulfide heterojunction photocatalysts with well-defined interfaces for direct Z-scheme water splitting under visible light, ChemSusChem 13 (2020) 2996–3004.
[5] C. Xu, Y. Kong, W. Zhang, M. Yang, K. Wang, L. Chang, W. Chen, G. Huang, J. Zhang, S-scheme 2D/2D $FeTiO_3$/g-C_3N_4 hybrid architectures as visible-light-driven photo-fenton catalysts for tetracycline hydrochloride degradation, Sep. Purif. Technol. 303 (2022), 122266.
[6] M.M.J. Sadiq, U.S. Shenoy, D.K. Bhat, Novel NRGO-$CoWO_4$-Fe_2O_3 nanocomposite as an efficient catalyst for dye degradation and reduction of 4-nitrophenol, Mater. Chem. Phys. 208 (2018) 112–122.
[7] H. Yang, Z. Zhao, Y. Yang, Z. Zhang, W. Chen, R. Yan, Defective WO_3 nanoplates controllably decorated with MIL-101(Fe) nanoparticles to efficiently remove tetracycline hydrochloride by S-scheme mechanism, Sep. Purif. Technol. 300 (2022), 121846.
[8] M. Zhang, C. Lai, B. Li, D. Huang, G. Zeng, P. Xu, L. Qin, S. Liu, X. Liu, H. Yi, M. Li, C. Chu, Z. Chen, Rational design 2D/2D BiOBr/CDs/g-C_3N_4 Z-scheme heterojunction photocatalyst with carbon dots as solid-state electron mediators for enhanced visible and NIR photocatalytic activity: kinetics, intermediates, and mechanism insight, J. Catal. 369 (2018) 469–481.
[9] M.M.J. Sadiq, U.S. Shenoy, D.K. Bhat, Novel RGO-$ZnWO_4$-Fe_3O_4 nanocomposite as high performance visible light photocatalyst, RSC Adv. 6 (2016) 61821–61829.
[10] W. Bahnemann, M. Muneer, M.M. Haque, Titanium dioxide-mediated photocatalysed degradation of few selected organic pollutants in aqueous suspensions, Catal. Today 124 (2007) 133–148.
[11] P. Mitra, P. Banerjee, S. Chakrabarti, S. Bhattacharjee, Utilization of solar energy for photoreduction of industrial wastewater containing hexavalent chromium with zinc oxide semiconductor catalyst, Desalin. Water Treat. 51 (2013) 5451–5459.
[12] H. Bantawal, U.S. Shenoy, D.K. Bhat, Tuning photocatalytic activity of $SrTiO_3$ by varying the Sr/Ti Ratio: unusual effect of viscosity of synthetic medium, J. Phys. Chem. C 122 (2018) 20027–20033.
[13] Q. Gao, J. Meng, Y. Yang, Q. Lin, Y. Lu, X. Wei, J. Li, G. Han, Z. Zhang, Zirconium doping in calcium titanate perovskite oxides with surface nanostep structure for promoting photocatalytic hydrogen evolution, Appl. Surf. Sci. 542 (2021), 148544.
[14] D.K. Bhat, H. Bantawal, U.S. Shenoy, Rhodium doping augments photocatalytic activity of barium titanate: effect of electronic structure engineering, Nanoscale Adv. 2 (2020) 5688–5698.
[15] R. Guo, A. Yan, J. Xu, B. Xu, T. Li, X. Liu, T. Yi, S. Luo, Effects of morphology on the visible-light-driven photocatalytic and bactericidal properties of $BiVO_4$/CdS heterojunctions: a discussion on photocatalysis mechanism, J. Alloy. Compd. 817 (2020), 153246.
[16] J. Gan, X. Lu, Y. Tong, Towards highly efficient photoanodes: boosting sunlight-driven semiconductor nanomaterials for water oxidation, Nanoscale 6 (2014) 7142–7164.
[17] D. Cosma, A. Urda, T. Radu, M.C. Rosu, M. Mihet, C. Socaci, Evaluation of the photocatalytic properties of copper oxides/graphene/TiO_2 nanoparticles composites, Molecules 27 (2022) 1–14.
[18] T. Iqbal, A. Masood, N.R. Khalid, M.B. Tahir, A.M. Asiri, H. Alrobei, Green synthesis of novel lanthanum doped copper oxide nanoparticles for photocatalytic application: correlation between experiment and COMSOL simulation, Ceram. Int. 48 (2022) 13420–13430.
[19] V. Beena, S.L. Rayar, S. Ajitha, A. Ahmad, F.J. Iftikhar, K.M. Abualnaja, T. S. Alomar, M. Ouladsmne, S. Ali, Photocatalytic dye degradation and biological activities of Cu-doped ZnSe nanoparticles and their insights, Water 13 (2021) 2561.
[20] U.S. Shenoy, D.K. Bhat, Vanadium doped $BaTiO_3$ as high performance thermoelectric material: role of electronic structure engineering, Mater. Today Chem. 18 (2020), 100384.
[21] M. Nageri, V. Kumar, Manganese-doped $BaTiO_3$ nanotube arrays for enhanced visible light photocatalytic applications, Mater. Chem. Phys. 213 (2018) 400–405.
[22] S. Nishimoto, M. Matsuda, M. Miyake, Photocatalytic activities of Rh-doped $CaTiO_3$ under visible light irradiation, Chem. Lett. 35 (2006) 308–309.
[23] H. Yu, J. Wang, S. Yan, T. Yu, Z. Zou, Elements doping to expand the light response of $SrTiO_3$, J. Photochem. Photobiol. A 275 (2014) 65–71.
[24] J. Zhu, F. Chen, J. Zhang, H. Chen, M. Anpo, Fe^{3+}-TiO_2 Photocatalysts prepared by combining sol-gel method with hydrothermal treatment and their characterization, J. Photochem. Photobiol. A 180 (2016) 196–204.

[25] P. Demircivi, E.B. Simsek, Visible-light-enhanced photoactivity of perovskite-type W-doped $BaTiO_3$ photocatalyst for photodegradation of tetracycline, J. Alloy. Compd. 774 (2019) 795–802.
[26] M.A.M. Khan, S. Kumar, J. Ahmed, M. Ahamed, A. Kumar, Influence of silver doping on the structure, optical and photocatalytic properties of Ag-doped $BaTiO_3$ ceramics, Mater. Chem. Phys. 259 (2021), 124058.
[27] L.G. Devi, B.N. Murthy, Characterization of Mo doped TiO_2 and its enhanced photo catalytic activity under visible light, Catal. Lett. 125 (2008) 320–330.
[28] A.I.J. Joseph, S. Thiripuranthagan, Metal doped titanate photo catalysts for the mineralization of congo red under visible irradiation, RSC Adv. 5 (2015) 9792–9805.
[29] T. Xie, Y. Wang, C. Liu, L. Xu, New insights into sensitization mechanism of the doped Ce (IV) into strontium titanate, Materials 11 (2018) 1–17.
[30] J.P. Zou, L.Z. Zhang, S.L. Luo, L.H. Leng, X.B. Luo, M.J. Zhang, Y. Luo, G.C. Guo, Preparation and photocatalytic activities of two new Zn-doped $SrTiO_3$ and $BaTiO_3$ photocatalysts for hydrogen production from water without cocatalysts loading, Int. J. Hydrog. Energy 37 (2012) 17068–17077.
[31] Y. Ni, H. Zheng, N. Xiang, K. Yuan, J. Hong, Simple hydrothermal synthesis and photocatalytic performance of coral-like $BaTiO_3$ nanostructures, RSC Adv. 5 (2015) 7245–7252.
[32] Q.I. Rahman, M. Ahmad, S.K. Misra, M. Lohani, Efficient degradation of methylene blue dye over highly reactive Cu doped strontium titanate ($SrTiO_3$) nanoparticles photocatalyst under visible light, J. Nanosci. Nanotechnol. 12 (2012) 7181–7186.
[33] A. Rosy, G. Kalpana, Reduced graphene oxide/strontium titanate heterostructured nanocomposite as sunlight driven photocatalyst for degradation of organic dye pollutants, Curr. Appl. Phys. 18 (2018) 1026–1033.
[34] P.I. Uma, U.S. Shenoy, D.K. Bhat, Electronic structure engineering of $BaTiO_3$ cuboctahedrons by doping copper to enhance the photocatalytic activity for environmental remediation, J. Alloy. Compd. 948 (2023), 169600.
[35] U.S. Shenoy, H. Bantawal, D.K. Bhat, Band engineering of $SrTiO_3$: effect of synthetic technique and site occupancy of doped rhodium, J. Phys. Chem. C 122 (2018) 27567–27574.
[36] M.M.J. Sadiq, U.S. Shenoy, D.K. Bhat, $NiWO_4$-ZnO-NRGO ternary nanocomposite as an efficient photocatalyst for degradation of methylene blue and reduction of 4-nitro phenol, J. Phys. Chem. Solids 109 (2017) 124–133.
[37] P. Giannozzi, S. Baroni, N. Bonini, M. Calandra, R. Car, C. Cavazzoni, D. Ceresoli, G.L. Chiarotti, M. Cococcioni, I. Dabo, A. Dal Corso, S. de Gironcoli, S. Fabris, G. Fratesi, R. Gebauer, U. Gerstmann, C. Gougoussis, A. Kokalj, M. Lazzeri, L. Martin-Samos, N. Marzari, F. Mauri, R. Mazzarello, S. Paolini, A. Pasquarello, L. Paulatto, C. Sbraccia, S. Scandolo, G. Sclauzero, A.P. Seitsonen, A. Smogunov, P. Umari, R.M. Wentzcovitch, Quantum ESPRESSO: a modular and open-source software project for quantum simulations of materials, J. Phys. Condens. Matter 21 (2009), 395502.
[38] J.P. Perdew, K. Burke, M. Ernzerhof, Generalized gradient approximation made simple, Phys. Rev. Lett. 77 (1996) 3865.
[39] M.M.J. Sadiq, U.S. Shenoy, D.K. Bhat, Synthesis of $BaWO_4$/NRGO–g-C_3N_4 nanocomposites with excellent multifunctional catalytic performance via microwave approach, Front. Mater. Sci. 12 (2018) 247–263.
[40] H. Bantawal, M. Sethi, U.S. Shenoy, D.K. Bhat, Porous graphene wrapped $SrTiO_3$ nanocomposite: Sr-C bond as an effective coadjutant for high performance photocatalytic degradation of methylene blue, ACS Appl. Nano Mater. 2 (2019) 6629–6636.
[41] I.C. Amaechi, A. Hadj Youssef, D. Rawach, J.P. Claverie, S. Sun, A. Ruediger, Ferroelectric Fe-Cr Codoped $BaTiO_3$ nanoparticles for the photocatalytic oxidation of azo dyes, ACS Appl. Nano Mater. 2 (2019) 2890–2901.
[42] M. Sethi, U.S. Shenoy, D.K. Bhat, Porous graphene-$NiCo_2O_4$ nanorod hybrid composite as a high performance supercapacitor electrode material, New J. Chem. 44 (2020) 4033–4041.
[43] D.S.D. Lima, J.C. Cruz, V.A. Luciano, M.A. Nascimento, A.P.C. Teixeira, R.P. Lopes, Enhanced photocatalytic activity of cobalt-doped titanate nanotube heterostructures decorated with Cu_2O-CuO nanoparticles for organic pollutant degradation under UV and visible irradiation, Appl. Surf. Sci. 563 (2021), 150313.
[44] X.J. Yang, S. Wang, H.M. Sun, X.B. Wang, J.S. Lian, Preparation and photocatalytic performance of Cu-doped TiO_2 nanoparticles, Trans. Nonferr. Met. Soc. China 25 (2015) 504–509.
[45] M. Sethi, U.S. Shenoy, D.K. Bhat, A Porous Graphene-$NiFe_2O_4$ nanocomposite with high electrochemical performance and high cycling stability for energy storage applications, Nanoscale Adv. 2 (2020) 4229–4241.
[46] D.K. Bhat, U.S. Shenoy, Zn: a versatile resonant dopant for SnTe thermoelectrics, Mater. Today Phys. 11 (2019), 100158.
[47] U.S. Shenoy, D.K. Bhat, Electronic structure engineering of $SrTiO_3$ via rhodium doping: a DFT study, J. Phys. Chem. Solids 148 (2021), 109708.
[48] U.S. Shenoy, D.K. Bhat, Enhanced thermoelectric properties of vanadium doped $SrTiO_3$: a resonant dopant approach, J. Alloy. Compd. 832 (2020), 154958.
[49] P. Makuła, M. Pacia, W. Macyk, How to correctly determine the band gap energy of modified semiconductor photocatalysts based on UV–vis spectra, J. Phys. Chem. Lett. 9 (2018) 6814–6817.
[50] M. Abdi, V. Mahdikhah, S. Sheibani, Visible light photocatalytic performance of La-Fe Co-doped $SrTiO_3$ perovskite powder, Opt. Mater. 102 (2020), 109803.
[51] H. Bantawal, U.S. Shenoy, D.K. Bhat, Vanadium doped $CaTiO_3$ cuboids: role of vanadium in improving the photocatalytic activity, Nanoscale Adv. 3 (2021) 5301–5311.
[52] S. Sharma, R. Ameta, R.K. Malkani, S.C. Ameta, Photocatalytic degradation of rose bengal using semiconducting zinc sulphide as the photocatalyst, J. Serb. Chem. Soc. 78 (2013) 897–905.
[53] U.G. Akpan, B.H. Hameed, Parameters affecting the photocatalytic degradation of dyes using TiO_2-based photocatalysts: a review, J. Hazard. Mater. 170 (2009) 520–529.
[54] R.S. Dariani, A. Esmaeili, A. Mortezaali, S. Dehghanpour, Photocatalytic reaction and degradation of methylene blue on TiO_2 nano-sized particles, Optik 127 (2016) 7143–7154.
[55] Z. Yu, S.S.C. Chuang, Probing methylene blue photocatalytic degradation by adsorbed ethanol with *in situ* IR, J. Phys. Chem. C 111 (2007) 13813–13820.